galaxies

Tracked for Impact Factor

CITESCORE 3.3

Article

Neutron Star Radii, Deformabilities, and Moments of Inertia from Experimental and Ab Initio Theory Constraints of the ^{208}Pb Neutron Skin Thickness

Yeunhwan Lim and Jeremy W. Holt

Special Issue

Neutron Stars and Hadrons in the Era of Gravitational Wave Astrophysics

Edited by

Dr. Plamen G. Krastev

MDPI

https://doi.org/10.3390/galaxies10050099

galaxies

MDPI

Article

Neutron Star Radii, Deformabilities, and Moments of Inertia from Experimental and Ab Initio Theory Constraints of the ^{208}Pb Neutron Skin Thickness

Yeunhwan Lim [1,*] and Jeremy W. Holt [2,3]

[1] Department of Science Education, Ewha Womans University, Seoul 03760, Korea
[2] Cyclotron Institute, Texas A&M University, College Station, TX 77843, USA
[3] Department of Physics and Astronomy, Texas A&M University, College Station, TX 77843, USA
* Correspondence: yeunhwan.lim@ewha.ac.kr

Abstract: Recent experimental and ab initio theory investigations of the ^{208}Pb neutron skin thickness have the potential to inform the neutron star equation of state. In particular, the strong correlation between the ^{208}Pb neutron skin thickness and the pressure of neutron matter at normal nuclear densities leads to modified predictions for the radii, tidal deformabilities, and moments of inertia of typical 1.4 $M_\odot$ neutron stars. In the present work, we study the relative impact of these recent analyses of the ^{208}Pb neutron skin thickness on bulk properties of neutron stars within a Bayesian statistical analysis. Two models for the equation of state prior are employed in order to highlight the role of the highly uncertain high-density equation of state. From our combined Bayesian analysis of nuclear theory, nuclear experiment, and observational constraints on the dense matter equation of state, we find at the 90% credibility level $R_{1.4} = 12.36^{+0.38}_{-0.73}$ km for the radius of a 1.4 $M_\odot$ neutron star, $R_{2.0} = 11.96^{+0.94}_{-0.71}$ km for the radius of a 2.0 $M_\odot$ neutron star, $\Lambda_{1.4} = 440^{+103}_{-144}$ for the tidal deformability of a 1.4 $M_\odot$ neutron star, and $I_{1.338} = 1.425^{+0.074}_{-0.146} \times 10^{45}$ g cm^2 for the moment of inertia of PSR J0737-3039A whose mass is 1.338 $M_\odot$.

Keywords: neutron stars; nuclear equation of state; chiral effective field theory

Citation: Lim, Y.; Holt, J.W. Neutron Star Radii, Deformabilities, and Moments of Inertia from Experimental and Ab Initio Theory Constraints of the ^{208}Pb Neutron Skin Thickness. *Galaxies* **2022**, *10*, 99. https://doi.org/10.3390/galaxies10050099

Academic Editor: Plamen G. Krastev

Received: 3 June 2022
Accepted: 8 September 2022
Published: 20 September 2022

1. Introduction

Neutron stars have attracted a great deal of attention in recent years as new measurements of masses from radio pulsar timing [1–3], tidal deformabilities from gravitational wave analyses [4,5], and radii from X-ray pulse profiling [6–9] have begun to clarify the possible existence of novel states of matter in the dense inner cores of the heaviest neutron stars and the equation of state of dense matter [10–12]. At the same time, progress in nuclear effective field theories [13,14] have enabled similarly strong constraints [12,15–22] on the dense matter equation of state and bulk properties of typical 1.4 $M_\odot$ neutron stars. These nuclear theory models can be further refined through precise investigations of neutron-rich nuclei, which probe the density dependence of the nuclear isospin-asymmetry energy that characterizes the energy cost of converting protons into neutrons in a nuclear many-body medium. Recently, the PREX-II experimental measurement [23,24] of the ^{208}Pb neutron skin thickness $R_{np} \equiv R_n - R_p = (0.283 \pm 0.071)$ fm has provided new insights into the nuclear isospin-asymmetry energy, which can then be combined with neutron star observations in comprehensive statistical analyses [10,25] of the dense matter equation of state. One finds that on one side, measurements of neutron star tidal deformabilities from merging binaries and nuclear theory calculations based on chiral effective field theory tend to favor soft equations of state around $1-2\,n_0$, where n_0 is the nuclear matter saturation density. On the other side, NICER radius measurements and the PREX-II neutron skin thickness measurement of ^{208}Pb tend to favor stiff equations of state. Even more recently, ab initio nuclear theory calculations [26] have predicted a significantly smaller neutron skin thickness

$R_n - R_p = (0.14 - 0.20)$ fm of ^{208}Pb, which is consistent with the soft equations of state found from previous chiral effective field theory investigations. The goal of the present work is to systematically study the relative impact of these ^{208}Pb neutron skin thickness analyses together with other theory, experimental, and astrophysical constraints on the dense matter equation of state, all within a Bayesian statistical framework. We will show that our posterior probability distributions for the neutron star equation of state remain relatively broad, even under the assumption of a smooth extrapolation from low to very high densities, where the composition of neutron stars remains highly uncertain.

One of the strongest constraints on exotic states of matter in neutron star interiors comes from neutron star mass measurements. For instance, the observation of $\sim 2\,M_\odot$ neutron stars [1–3] strongly disfavors [27,28] the appearance of strangeness in neutron stars at around $2 - 3\,n_0$, the canonical density inferred from a variety of hyperon–nucleon two-body forces [29,30]. To resolve this apparent tension, it is natural to investigate the role of the more uncertain hyperon–nucleon–nucleon three-body forces [31], which can delay [28,32] the onset of strangeness in neutron stars, perhaps even indefinitely.

Observations of gravitational waves from the late-inspiral phase of GW170817 strongly favor small tidal deformabilities for $1.4\,M_\odot$ neutron stars, $\Lambda_{1.4} = 190^{+390}_{-120}$ [4,5,33], and hence soft equations of state around twice the nuclear matter saturation density $2n_0$. In order to infer the existence of a phase transition at high densities, it may be more promising to observe gravitational waves from the post-merger phase of binary neutron star coalescence and in particular the oscillation frequencies of hypermassive neutron star remnants. Neutron star equations of state with only lepton and nucleon degrees of freedom show a strong correlation between the peak frequency of the oscillating remnant and the radius or tidal deformability of typical $1.4\,M_\odot$ neutron stars [34]. Strong deviations from this speculated correlation could indicate the presence of a phase transition to a hybrid quark-hadron star. For most neutron star merger events, however, current gravitational wave detectors do not have sufficient sensitivity in the high-frequency band above 1kHz to measure remnant oscillations.

Neutron star radii and tidal deformabilities are strongly correlated. From GW170817 one can already place an upper bound $R_{1.4} \lesssim 13.5\,\text{km}$ on the radius of $1.4\,M_\odot$ neutron stars [5,16,35]. More direct measurements of neutron star radii from X-ray pulse profiling [6–9] are consistent with inferences from GW170817, but statistically favor somewhat larger radii. In the case of the NICER X-ray measurements of PSR J0030+0451, two independent analyses found $M = 1.44^{+0.15}_{-0.14} M_\odot$ and $R = 13.02^{+1.24}_{-1.06}\,\text{km}$ [6] and $M = 1.34^{+0.15}_{-0.16} M_\odot$ and $R = 12.71^{+1.14}_{-1.19}\,\text{km}$ [7] at the 68% credibility level. Furthermore, the recent results from NICER-XMM for PSR J0740+6620 also support the stiff EOS scenario. The radius of this $2.08\,M_\odot$ neutron star is predicted to be $R_{2.08} = 13.7^{+2.6}_{-1.5}\,\text{km}$ from Miller et al. [8] and $R_{2.08} = 12.39^{+1.30}_{-0.98}\,\text{km}$ from Riley et al. [9]. One possibility to infer the existence of a phase transition at high density from radius measurements is to search for so called "twin stars", that is, two neutron stars with similar gravitational mass but different radii, which would provide strong evidence for a third stable branch of cold dense stars (after white dwarfs and neutron stars) [36]. Present uncertainties in neutron star radius measurements, however, are likely still too large to be able to resolve hypothetical twin stars.

Complementary to the progress that has taken place in neutron star observations and astrophysics simulations, theoretical modeling of neutron stars based on state-of-the-art nuclear forces have reached sufficient accuracy to strongly constrain the neutron star equation of state and the associated properties of light $\sim 1.4\,M_\odot$ neutron stars [18,19]. For instance, in Ref. [15] chiral effective field theory calculations of the neutron matter equation of state up to nuclear matter saturation density n_0 were used to predict that the radius of a $1.4\,M_\odot$ neutron star lies in the range $9.7\,\text{km} < R_{1.4} < 13.9\,\text{km}$. Later, in Ref. [18] it was shown that, by combining chiral effective field theory, priors on the dense matter equation of state together with likelihood functions obtained from isovector properties of medium-mass and heavy nuclei, $R_{1.4}$ lies in the range $10.4\,\text{km} < R_{1.4} < 12.9\,\text{km}$ and the tidal deformability for $1.4\,M_\odot$ neutron stars lies in the range $140 < \Lambda_{1.4} < 520$ (see also

Ref. [19] for a similar study of the binary tidal deformability parameter $\tilde{\Lambda}$ associated with GW170817). Low-density constraints from chiral effective field theory have also enabled more refined predictions of neutron star radii [20,37] and moments of inertia [38,39].

Isovector properties of medium-mass and heavy nuclei provide a third avenue to infer the empirical parameters of the nuclear equation of state around the saturation density n_0. For instance, the combination of experimentally measured masses, neutron skins, giant dipole resonances, and dipole polarizabilities has provided a strong constraint [40,41] on the nuclear isospin-asymmetry energy, with uncertainties comparable to that of recent chiral effective field theory calculations [42–44]. In addition, heavy-ion collisions [45–47] can give insights into the equation of state at supra-saturation densities. Recently, the measurement [23] of the parity-violating asymmetry in the elastic scattering of longitudinally polarized electrons off ^{208}Pb has provided new constraints [24,48] on the neutron skin thickness of ^{208}Pb and the symmetry energy slope parameter L, though the extraction of the latter quantity requires model assumptions. For instance, Refs. [23,24] report the constraints $R_n - R_p = 0.283 \pm 0.071$ fm and $L = 106 \pm 37$ MeV, while Ref. [48] reports $R_n - R_p = 0.19 \pm 0.02$ fm and $L = 54 \pm 8$ MeV using a wider class of energy density functionals and including also the experimentally measured electric dipole polarizability of ^{208}Pb as a constraint. In addition, the recent ab initio nuclear theory calculation [26] of the neutron skin thickness of ^{208}Pb has obtained $R_n - R_p = 0.14 - 0.20$ fm, which is much closer to the experimental evaluation in Ref. [48].

In light of these recent novel nuclear experiments, ab initio nuclear theory calculations, and neutron star observations, we study their relative impact on the dense matter equation of state and derived properties of neutron stars. Given the highly uncertain nature of the composition and pressure of ultra-dense matter beyond about twice nuclear saturation density, we employ two different prior probability distributions in our analysis. Both are based on the work of Refs. [18,49], where chiral EFT calculations at varying cutoff scale and order in the chiral expansion are first used to construct a probability distribution of energy density functionals. These models are then further constrained by empirical information on nuclear matter properties around saturation density inferred from studies of medium-mass and heavy nuclei. Up to twice nuclear matter saturation density, our two prior distributions are identical. Beyond $2n_0$, our first prior probability distribution assumes a smooth extrapolation of the functional form obtained at lower densities. Our second prior model assumes a transition to the maximally-stiff equation of state, where the speed of sound is equal to the speed of light, at a transition density n_c that is uniformly varied in the range $2n_0 < n_c < 4n_0$. Taken together, the two models may be used to infer potential breakdowns in the chiral effective field theory description of nuclear interactions and the possible existence of phase transitions at supra-saturation density.

The paper is organized as follows. In Section 2 we provide a description of our neutron star modeling, which explicitly accounts for the physics of the outer and inner crusts. In Section 3 we describe details of the Bayesian statistical modeling used to account for constraints from ab initio nuclear theory, nuclear experiment, and neutron star observations. In Section 4 we present results for the nuclear equation of state and derived neutron star properties based on our propagated likelihood functions. We end with a summary and discussion.

2. Neutron Star Modeling

Many qualitative features of neutron star structure are well understood and do not depend sensitively on the choice of nuclear force model used to generate the equation of state. The neutron star crust consists of ionized heavy nuclei with the possibility of unbound neutrons beyond a transition density set by the neutron chemical potential. This inhomogeneous phase of nuclear matter exists until the total baryon number density increases to approximately one-half saturation density [50], at which point the lattice structure melts to a fluid of protons, neutrons, and electrons, a state of matter that has a lower energy than the inhomogeneous phase. The effects of three-nucleon forces already

begin to play a role close to the crust–core transition density, and the uncertainties in chiral EFT calculations of uniform neutron matter begin to increase considerably at around half saturation density, regardless of the many-body method employed (e.g., many-body perturbation theory [42,51–55], quantum Monte Carlo [56–59], or self-consistent Green's function theory [60]). In addition, uncertainties in the symmetric nuclear matter equation of state, especially regarding the saturation energy and density, impact the crust-core transition density. However, the transition density does not depend on the mass of the neutron star.

The region of a neutron star below the crust is traditionally divided into an "outer core" and "inner core", where the transition to the inner core is accompanied by the appearance of novel degrees of freedom beyond protons, neutrons, electrons, and muons (the latter arise when the electron chemical potential surpasses the rest mass of the muon, 105.7 MeV). For instance, in the inner core, the ground state of dense matter might be comprised of hyperons, meson condensates, or deconfined quarks. Since the existence of such exotic states of matter is not certain, especially in light of observed heavy $\sim 2\,M_\odot$ neutron stars, the neutron star inner core remains highly speculative.

Although the general composition of the neutron star outer core is well understood, its detailed properties (e.g., proton fraction or pressure as a function of density) depend sensitively on the nuclear force. In the outer core, the nuclear equation of state can be constrained from nuclear experiments, nuclear theory, and astrophysical observations. Currently, there are more than 2300 nuclei whose masses are measured [61] and which provide a strong constraint on the nuclear matter saturation energy B, saturation density n_0, and incompressibility K. Pure neutron matter cannot be studied directly in the laboratory, but at low to moderate densities up to $\sim 2n_0$ chiral effective field theory can provide strong constraints on the neutron matter equation of state [42,51,62]. In the following we will derive properties of neutron stars through parametric modeling of the equation of state from chiral effective field theory and nuclear experiments.

2.1. Neutron Star Equation of State

The mass–radius relation for non-rotating neutron stars can be obtained by solving the TOV equations,

$$\begin{aligned} \frac{dp}{dr} &= -\frac{[M(r) + 4\pi r^3 p](\varepsilon + p)}{r[r - 2M(r)]}\,, \\ \frac{dM}{dr} &= 4\pi\varepsilon r^2\,, \end{aligned} \tag{1}$$

where p and ε are the pressure and total energy density, r is the distance from the center, and $M(r)$ is the enclosed mass of a neutron star at the distance r from the center. Note that we use units where $G = 1$ and $c = 1$. The nuclear physics inputs are therefore the energy density ε and pressure p, which are related through the equation of state. Since the pressure is given by the derivative of the energy density with respect to the baryon number density, we can regard the EOS as the energy density for a given baryon number density.

In principle, one can approximate the equation of state of isospin-symmetric nuclear matter through a Taylor series expansion around saturation density n_0:

$$A_0(n) = -B + \frac{K}{9}\left(\frac{n - n_0}{n_0}\right)^2 + \frac{Q}{27}\left(\frac{n - n_0}{n_0}\right)^3 + \cdots\,, \tag{2}$$

where B is the (positive) binding energy of nuclear matter at the saturation density, K is the incompressibility, and Q is the skewness parameter. One may similarly expand the equation of state for asymmetric nuclear matter about the isospin-symmetric point, however, in addition to the normal even powers of the isospin asymmetry $\delta_{np} = (n_n - n_p)/(n_n + n_p)$ one also finds [54,63] nonanalytic logarithmic terms in the combined expansion

$$\frac{E}{N}(n,\delta_{np}) = A_0(n) + S_2(n)\delta_{np}^2 + \sum_{i=2}^{\infty}(S_{2i}(n) + L_{2i}(n)\ln|\delta_{np}|)\delta_{np}^{2n} \tag{3}$$

when the equation of state is computed at least to second order in perturbation theory. Although the above expansion in Equation (3) was originally derived [63] assuming a zero-range contact interaction, detailed calculations [64] have demonstrated that realistic nuclear forces do not give rise to any additional nonanalytic terms. One also finds [53,54,64–66] that the expansion in Equation (3) is dominated by the leading term $S_2(n)$, referred to as the isospin-asymmetry energy, which like Equation (2) can be expanded about nuclear saturation density:

$$S_2(n) = J + \frac{L}{3}\left(\frac{n-n_0}{n_0}\right) + \frac{K_{\rm sym}}{9}\left(\frac{n-n_0}{n_0}\right)^2 + \frac{Q_{\rm sym}}{27}\left(\frac{n-n_0}{n_0}\right)^3 + \cdots . \tag{4}$$

Although useful for orientation, neither Equation (2) nor (4) is generally well converged at high densities beyond $2n_0$. Thus, we model the equation of state of homogeneous matter using energy density functionals, where the energy density is given as a function of the baryon number density n and proton fraction x:

$$\mathcal{E}(n,x) = \frac{1}{2m}\tau_n + \frac{1}{2m}\tau_p + (1-2x)^2 f_n(n) + [1-(1-2x)^2] f_s(n), \tag{5}$$

where

$$f_n(n) = \sum_{i=0}^{3} a_i n^{2+i/3}, \quad f_s(n) = \sum_{i=0}^{3} b_i n^{2+i/3}. \tag{6}$$

In the above functional, f_n (f_s) represents the potential energy for pure neutron matter (symmetric nuclear matter). Note that $n^{1/3} \sim k_F$ is used for the expansion instead of integer powers of n for the smooth fit to microscopic calculations.

In chiral effective field theory, the short-distance part of the nuclear force is encoded in a set of two-nucleon (2N) and three-nucleon (3N) low-energy constants that are typically fitted to 2N and 3N scattering, reaction, and bound-state observables only. Therefore, theoretical predictions for the dense matter equation of state from chiral EFT can be used to generate a prior probability distribution for the parameters $\{a_i, b_i\}$ entering in Equation (6). In Ref. [18] we have used a set of five chiral interactions with varying momentum-space cutoff and order in the chiral expansion to calculate the neutron matter and symmetric nuclear matter equations of state at varying orders in many-body perturbation theory (up to third order [42]). The functional form in Equation (6) including four terms ($i = 0, 1, 2, 3$) in the power series was shown to be sufficient to fit the nuclear equation of state up to $2n_0$. Only small variations in the fitted parameters were observed when the maximal density was reduced to $1.5n_0$. We note that we do not consider correlations between the sets of $\{a_i\}$ and $\{b_i\}$ parameters, since our aim is to generate a relatively conservative estimate of the distribution. In contrast, recent work [67] has shown that such correlations can have an important impact on uncertainty estimates for derived quantities, such as the nuclear symmetry energy.

The binding energy of symmetric nuclear matter around the saturation density is a fine-tuned quantity, and therefore chiral effective field theory calculations tend to have sizeable uncertainties at and above saturation density. In particular, the tensor force generated by one-pion-exchange is a dominant feature in the spin-triplet interaction that contributes strongly to the uncertainty in the symmetric nuclear matter equation of state. In contrast,

the pure neutron matter equation of state receives only small contributions from the tensor force, since the $L = 0$ spin-triplet state is Pauli forbidden. One finds that the uncertainties in the symmetric nuclear matter and pure neutron matter equations of state around the saturation density are comparable, despite the fact that one may naively anticipate a poorer convergence of the neutron matter calculations since the neutron Fermi momentum is about 25% larger than in symmetric nuclear matter.

The probability distribution for the equation of state parameters in Equation (6) can be significantly reduced by combining the prior distribution with likelihood functions that include experimental data from medium-mass and heavy nuclei. For this purpose, we take a set of 205 mean field models [68] fitted to the properties of finite nuclei and compute the derived constraints on the nuclear matter empirical parameters. In the case of symmetric nuclear matter we employ empirical constraints on (i) the nuclear saturation density n_0, (ii) the binding energy per particle at saturation density B, (iii) the incompressibility K, and (iv) the skewness parameter Q in Equation (2). Whereas the saturation properties are strongly constrained by known nuclear masses, the incompressibilty and especially the skewness parameter have larger uncertainties. We refer the reader to Ref. [20] for additional details, including plots of the empirical parameter distributions used in constructing the symmetric nuclear matter equation of state prior. In the case of pure neutron matter, we employ empirical constraints on J [41,69] together with universal correlations among J, L, $K_{\rm sym}$, and $Q_{\rm sym}$ observed in Refs. [70,71]. Additional details can again be found in Ref. [20], where for instance it is shown that the symmetry energy slope parameter L lies in the range $20\,\text{MeV} < L < 90\,\text{MeV}$, which is sufficiently flexible to accommodate additional constraints from e.g., the PREX-II experiment.

2.2. Uniform Nuclear Matter

Our posterior probability distribution for the equation of state parameterization in Equation (6) is only constrained in a relatively narrow region $0 < n < 2n_0$, where both chiral effective field theory calculations and finite nuclei properties are informative. However, the central density in the heaviest neutron stars can reach $5-10n_0$, and therefore we consider two separate models for the high-density equation of state. First, our "smooth extrapolation" extends the posterior probability distribution for the equation of state to the highest densities without modification. The only additional constraint we impose on this distribution is that the speed of sound cannot exceed the speed of light (such unphysical equations of state are removed from our modeling). Second, our "maximally stiff extrapolation" [49] probes the limiting case where the speed of sound achieves the maximal value of $c_s = c$ at and above a specified transition density n_c. This maximally stiff extrapolation allows one to probe the maximum neutron star mass consistent with low- to moderate-density constraints from nuclear physics and to draw model-independent conclusions about the density at which traditional nuclear physics models break down.

For the maximally stiff high-density extrapolation, we introduce a smooth jump in the speed of sound at the critical density n_c,

$$\frac{c_s^2}{c^2} = \begin{cases} 1 & \text{if} \quad \varepsilon > \varepsilon_c + \Delta_\varepsilon\,, \\ \tilde{c}_c^2 + \frac{1-\tilde{c}_c^2}{\Delta_\varepsilon}(\varepsilon - \varepsilon_c) & \text{if} \quad \varepsilon_c < \varepsilon < \varepsilon_c + \Delta_\varepsilon\,, \\ \chi\text{EFT} & \text{otherwise}\,, \end{cases} \tag{7}$$

where ε_c is the energy density at $n = n_c$ and $\tilde{c}_c^2$ is the speed of sound at $n = n_c$ in units of c^2. The parameter Δ_ε is set to $\frac{1}{10}\varepsilon_c$ for a rather smooth transition. In this work, we vary n_c from $2n_0$ to $4n_0$ to simulate the effects on the neutron star mass-radius relation, tidal deformabilities, and moments of inertia. From the definition of the speed of sound $c_s^2/c^2 = \frac{\partial p}{\partial \varepsilon}$, we can obtain the pressure and baryon number density, which is necessary for solving the TOV equations. The pressure in the phase transition region, i.e., between ε_c and $\varepsilon_c + \Delta_\varepsilon$, is given by

$$p = p_c + \tilde{c}_c^2(\varepsilon - \varepsilon_c) + \frac{1 - \tilde{c}_c^2}{2\Delta_\varepsilon}(\varepsilon - \varepsilon_c)^2 . \tag{8}$$

Note that ε is an independent variable, and the pressure is simply determined by the relation between $\tilde{c}_c^2$ and ε.

2.3. Neutron Star Crust

The neutron star crust consists of nuclear clusters, i.e., ionized heavy nuclei, which have a lower ground state energy than homogeneous matter at the same density. In addition, neutrons may drip out of heavy nuclei as the total baryon number density increases or more nucleons are added to a fixed volume of box. In this case, the total energy density ($F_{\rm tot}$) consists of the internal energy of heavy nuclei (F_H), the internal energy of neutrons (F_o), the electron contribution (F_e), the Coulomb interaction (F_C) between protons and electrons, and the surface energy ($F_{\rm Surf}$) to make the non-uniform nuclear density profile. Therefore, the ground state configuration is obtained by minimizing the total energy density for a given baryon number density;

$$\begin{aligned} F_{\rm tot} &= F_H + F_C + F_{\rm Surf} + F_o + F_e \\ &\quad + \lambda_1[n - un_i - (1-u)n_{no}] \\ &\quad + \lambda_2[nY_p - un_i x_i] + \lambda_3[nY_p - n_e] , \end{aligned} \tag{9}$$

where u is the volume fraction of a heavy nucleus in the Wigner–Seitz cell for the numerical calculation, n (n_e) is the total baryon (electron) number density in the Wigner–Seitz cell, n_i is the baryon number density of a heavy nucleus, Y_p is the proton fraction in the Wigner-Seitz cell, n_{no} is the neutron number density, and λ_1, λ_2, and λ_3 are the Lagrange multipliers necessary for the energy minimization [50]. In detail, the contributions to the free energy density are given as

$$\begin{aligned} F_H &= un_i f_i, \\ F_C &= 2\pi(n_i x_i e r_N)^2 u f_d(u), \\ F_{\rm Surf} &= \frac{\sigma(x_i) u d}{r_N}, \\ F_o &= (1-u)n_{no} f_o, \\ F_e &= \frac{m_e^4}{8\pi^2}\chi(x_e) . \end{aligned} \tag{10}$$

In the electron energy density, $x_e = \frac{p_{f_e}}{m_e}$, p_{f_e} is the electron Fermi momentum and m_e is the mass of electron. The function $\chi(x_e)$ is given by

$$\chi(x_e) = \left\{ x_e(1 + x_2^2)^{1/2}(1 + 2x^2) - \ln[x + (1 + x^2)^{1/2}] \right\}.$$

At equilibrium all quantities are obtained by solving $\frac{\partial F_{\rm tot}}{\partial u} = 0$, $\frac{\partial F_{\rm tot}}{\partial n_i} = 0$, $\frac{\partial F_{\rm tot}}{\partial x_i} = 0$, $\frac{\partial F_{\rm tot}}{\partial Y_p} = 0$, $\frac{\partial F_{\rm tot}}{\partial n_{no}} = 0$, $\frac{\partial F_{\rm tot}}{\partial n_e} = 0$, $\frac{\partial F_{\rm tot}}{\partial \lambda_1} = 0$, $\frac{\partial F_{\rm tot}}{\partial \lambda_2} = 0$, and $\frac{\partial F_{\rm tot}}{\partial \lambda_3} = 0$. Note that the energy density involving the Coloumb and surface energy can be combined into one energy density $F_{CS} = F_C + F_{\rm Surf}$ from nuclear virial theorem ($2F_C = F_{\rm Surf}$) [72]. The transition from inhomogeneous matter to uniform nuclear matter is found by comparing the energy density differences in this formalism.

3. Bayesian Statistical Analysis

Neutron star properties such as radii, tidal deformabilities, and moments of inertia can be constrained by nuclear theory calculations, nuclear experiments, and astrophysical observations. Bayes' theorem states

$$P(M_i|D) = \frac{P(D|M_i)P(M_i)}{\sum_j P(D|M_j)P(M_j)} \tag{11}$$

where M_i are the equation of state model parameters, i.e., the set of $\{a_i\}$ and $\{b_i\}$ in Equation (6), $P(M_i)$ is the prior probability distribution for $\{a_i\}$ and $\{b_i\}$, D is the data which are independent of $\{a_i\}$ and $\{b_i\}$, and $P(D|M_i)$ is the likelihood. Here the independence implies that we assume no correlation between D and M_i before we obtain the final posterior distribution. In the present work, we implement the following data $D = \{$PREX-II, $R_{np}^{\rm th}(^{208}\mathrm{Pb})$, GW170817, NICER I, NICER II$\}$, which correspond respectively to the neutron skin thickness measurement from Ref. [23], the ab initio neutron skin thickness prediction from Ref. [26], the neutron star tidal deformability constraints from GW170817 [5], the simultaneous mass-radius measurement of PSR J0030+0451 [6,7], and the NICER-XMM radius measurement of PSR J0740+6620 [8,9].

For the $R_{np}^{\rm exp}(^{208}\mathrm{Pb})$ PREX-II measurement, we use the constraint on the slope parameter of the nuclear isospin-asymmetry energy from Reed et al. [24]:

$$\mathcal{L}^{\rm PREX-II} = \frac{1}{\sqrt{2\pi}\sigma_L} \exp\left[-\frac{(L-\langle L\rangle)^2}{2\sigma_L^2}\right], \tag{12}$$

where $\langle L\rangle = 106\,\mathrm{MeV}$ and $\sigma_L = 37\,\mathrm{MeV}$. Although the central value of L from the analysis in Ref. [24] appears inconsistent with previous analyses [10,20,41,67,69,73], the $R_{np}^{\rm exp}(^{208}\mathrm{Pb})$ measurement and model-dependent extraction of L show large uncertainties, i.e., $\sigma_L = 37\,\mathrm{MeV}$. Thus the 95% confidence interval ($32\,\mathrm{MeV} < \mathrm{L} < 180\,\mathrm{MeV}$) covers almost all previous results. In comparison, the ab initio theory prediction $R_{np}^{\rm th}(^{208}\mathrm{Pb})$ [26] of the neutron skin thickness is linked with various nuclear force parameters so that nuclear matter properties such as the binding energy, saturation density, incompressibility, symmetry energy, and its slope parameters are correlated. In Ref. [26], the symmetry energy is defined as the energy difference between pure neutron matter and symmetric nuclear matter at the nuclear saturation density, which in their calculations can vary between 0.14–0.18 fm^{-3}. Thus it is necessary to construct a three-dimensional kernel density estimate (KDE) for a given set of density, symmetry energy, and slope parameter with corresponding likelihood

$$\mathcal{L}^{R_{np}^{\rm th}(^{208}\mathrm{Pb})} = P(n_0, S_v, L)\,, \tag{13}$$

where $P(n_0, S_v, L)$ is the 3D-KDE from the analysis of Hu et al. [26].

On the astrophysical side, analysis of the gravitational waves from the neutron star merger event GW170817 [74] provides a likelihood by integrating the allowed range of the neutron star mass for a given neutron star EOS,

$$\mathcal{L}^{GW} = \int f(M_1, \Lambda_1, M_2, \Lambda_2)\, dM_1 dM_2\,, \tag{14}$$

where $f(M_1, \Lambda_1, M_2, \Lambda_2)$ is a four-dimensional probability. Since the EDF employed in this work determines the tidal deformability Λ, it is not necessary to perform the Λ_1 and Λ_2 integrals. The results from NICER I [6,7] and NICER II [8,9] provide posterior samples from the joint mass-radius distribution $f(M, R)$ that enters in the likelihood:

$$\mathcal{L}^{\rm NICERI,II} = \frac{1}{M_{\rm max} - M_{\rm start}} \int_{M_{\rm start}}^{M_{\rm max}} f(M, R)\, dM\,, \tag{15}$$

where $M_{\rm max}$ stands for the maximum mass of a neutron star for a given EOS. We set the starting mass $M_{\rm start}$ of a neutron star for the integration as $1M_\odot$, since the mass distribution of observed neutron stars has no weight below this value. In principle, another likelihood could come from observed heavy neutron stars [1,2]. However, the NICER analysis of PSR J0740+6620 [8,9] already places a strong constraint on the maximum neutron star mass. The final posterior probability is then given by

$$\mathcal{L} = \mathcal{L}^{\text{PREX-II}} \mathcal{L}^{R_{np}^{\text{th}}(^{208}\text{Pb})} \mathcal{L}^{\text{GW}} \mathcal{L}^{\text{NICERI}} \mathcal{L}^{\text{NICERII}} \mathcal{L}^{\text{prior}} . \quad (16)$$

From the above equation, we can obtain the probability or weight factor for each $(\vec{a}, \vec{b})$ associated with the neutron star equation of state.

4. Results

In Figure 1 we show the 99.5% confidence bands for the prior (blue) and posterior (red) neutron star equations of state for both the smooth (left) and maximally-stiff (right) high-density extrapolations. One observes that the main effect of neutron star observation and ^{208}Pb radius likelihood functions is to eliminate the softest equations of state from the smooth high-density prior. The maximally-stiff high-density prior shifts probabilistic weight from soft to stiff equations of state, resulting in 99.5% confidence bands on the equation of state that change very little with the inclusion of the various likelihood functions. One can conclude that our nuclear physics modeling based on chiral effective field theory and nuclear data built into the prior probability distributions already strongly constrains the neutron star equation of state and is consistent with current neutron star observations.

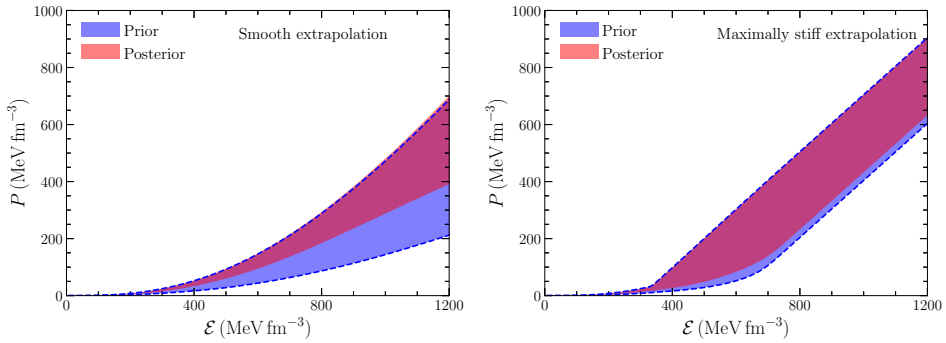

Figure 1. The 99.5% confidence intervals for the prior (blue) and posterior (light red) equations of state assuming a smooth high-density extrapolation (**left**) and a maximally-stiff high-density extrapolation (**right**).

Table 1 shows the average values of the prior and posterior energy density and pressure, i.e., (ε, p) at a given baryon number density $\{2n_0, 4n_0, 6n_0\}$. Since the lowest value of the critical density in the maximally-stiff EOS scenario is $2n_0$, there is almost no difference in the average (ε, p) values at $2n_0$ for the smooth and maximally-stiff extrapolations. One sees that the posterior EOS distributions peak at larger values of the pressure and energy in all cases. In addition, the maximally-stiff high-density extrapolation gives rise to larger average pressures and energy densities.

Table 1. Average values of energy density and pressure (ε, p) in units of MeV fm^{-3} at each baryon number density.

Number Density	$2n_0$	$4n_0$	$6n_0$
Prior (Smooth)	(312.76, 20.02)	(684, 152)	(1164, 483)
Prior (Stiff)	(312.76, 20.02)	(712, 280)	(1331, 897)
Post. (Smooth)	(313.60, 22.44)	(694, 175)	(1200, 560)
Post. (Stiff)	(313.23, 21.49)	(719, 296)	(1353, 929)

The posterior distribution of EDF parameters enables us to obtain various neutron star properties as well as nuclear matter properties. Figure 2 shows the correlations among the nuclear matter properties and neutron star properties from the posterior distribution in Equation (16), assuming the maximally-stiff high-density extrapolation for $\mathcal{L}^{\text{prior}}$. In the interest of brevity, we do not show the corner plot associated with the posterior distribution

derived from the smooth high-density extrapolation, which is very similar to that shown in Figure 2. At the top of each column in Figure 2 is the marginal probability distribution function associated with each of the given quantities. For example, the probability distribution for $R_{1.4}$ has a peak around 12.4 km and the probability decreases rapidly as $R_{1.4}$ increases. The left tail, on the other hand, reaches 11.63 km which is the left bound for the 90% credibility. Other plots in the first column show the correlation between $R_{1.4}$ and other neutron star properties and nuclear matter properties. In particular, one can see the very strong correlation between $\Lambda_{1.4}$ and $R_{1.4}$ which has already been analyzed in Refs. [16,18]. An even stronger correlation can be found between $R_{1.4}$ and $I_{1.338}$. Since the central densities for a 1.4 $M_\odot$ and a 1.338 $M_\odot$ neutron star are very close [20], the small difference in mass does not strongly affect the correlation. Both L and K_{sym} have strong correlations with $R_{1.4}$ and to a lesser extent $\Lambda_{1.4}$ and $I_{1.338}$. In contrast, the nuclear symmetry energy J is only weakly correlated with the bulk parameters of $\sim$1.4 $M_\odot$ neutron stars. We find that the radius of $\sim$2 $M_\odot$ neutron stars is not strongly correlated with any nuclear matter empirical parameter but instead can be constrained from more precise observations of radii, tidal deformabilities, or moments of inertia of $\sim$1.4 $M_\odot$ neutron stars.

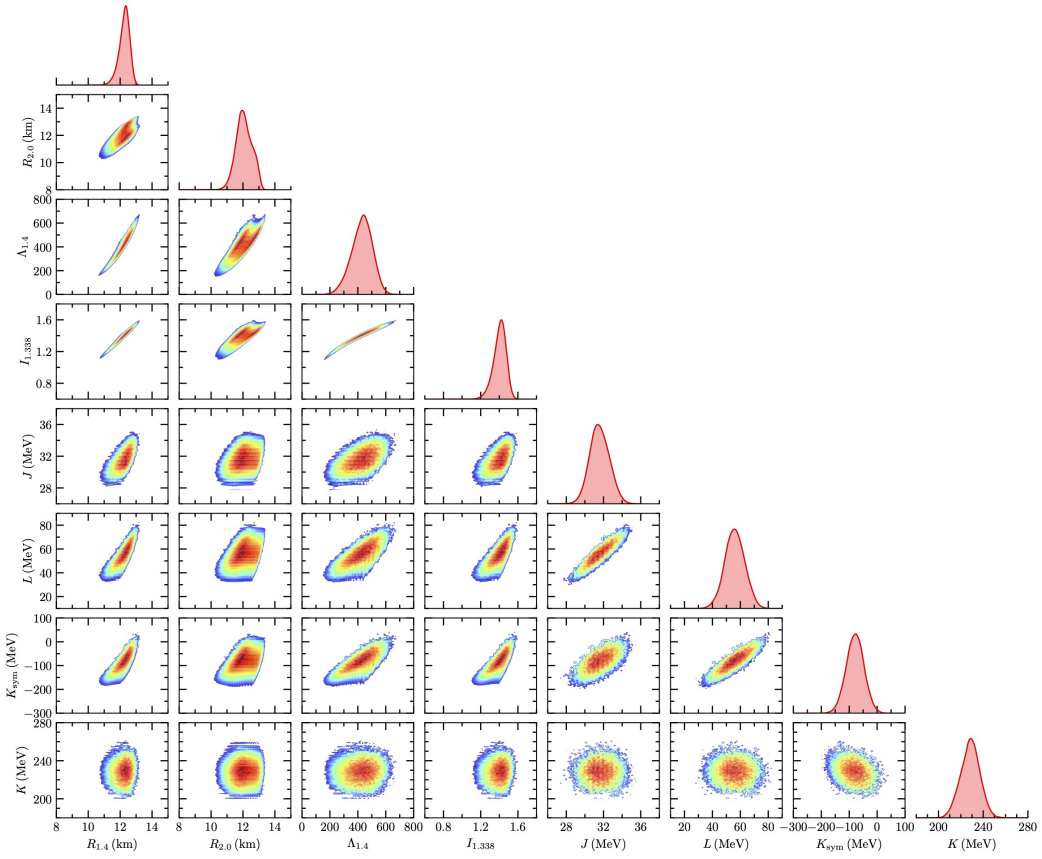

Figure 2. Correlations among neutron star properties and nuclear matter properties from the posterior probability distribution Equation (16) when the maximally-stiff high-density EOS extrapolation is used for $\mathcal{L}^{\rm prior}$. The colors in the 2D correlations represent the magnitude of the probability density, increasing from blue to red.

In Figure 3 we show the mass-radius probability distributions under the smooth high-density extrapolation (left subfigure) and the maximally-stiff high-density extrapolation (right subfigure). The subpanels within each subfigure show the constraints imposed on the mass-radius relation from each of the separate likelihood functions in Equation (16) as well as the combined posterior distribution labeled "All". We see that when all likelihood functions are implemented, the mass-radius confidence interval is highly reduced. In particular, the NICER II constraint (which simultaneously enforces a lower bound on the

maximum neutron star mass) has a strong impact on the posterior mass-radius relation in the "smooth extrapolation" scenario. This is due to the fact that chiral effective field theory predicts relatively soft equations of state, many of which lead to maximum neutron star masses less than $2\,M_\odot$. For the "maximally stiff" extrapolation, the NICER II constraint also eliminates the softest equations of state, but the stiff extrapolation naturally leads to heavier neutron stars more consistent with NICER II. The strongest reductions in the space of stiff equations of state come from GW170817 and the ab initio prediction $R_{np}^{\rm th}(^{208}{\rm Pb}) = 0.14 - 0.20\,{\rm fm}$ [26]. This theoretical calculation is ultimately based on a wide range of chiral nuclear forces, which are associated with soft equations of state. Despite the large central value of $R_{np}^{\rm exp}(^{208}{\rm Pb})$ (and the associated large value of the nuclear symmetry energy slope parameter L) from PREX-II, the sizeable uncertainty in the measurement only eliminates the softest equations of state from our modeling. The most likely probability region for the radius of a $1.4\,M_\odot$ neutron star in the case of the maximally stiff high-density extrapolation is somewhat larger than the case of the smooth extrapolation. This is due to the fact that many equations of state that are relatively soft for densities $n < 2n_0$ can nevertheless survive the likelihood functions that favor stiff equations of state due to the large increase in pressure after the transition density n_c. One therefore finds that smaller radii for $\sim 1.4\,M_\odot$ neutron stars are allowed in the maximally-stiff high-density extrapolation. The upper bound on the radii of $\sim 1.4\,M_\odot$ neutron stars is almost identical $R_{1.4} < 12.8\,{\rm km}$ under the two high-density EOS scenarios.

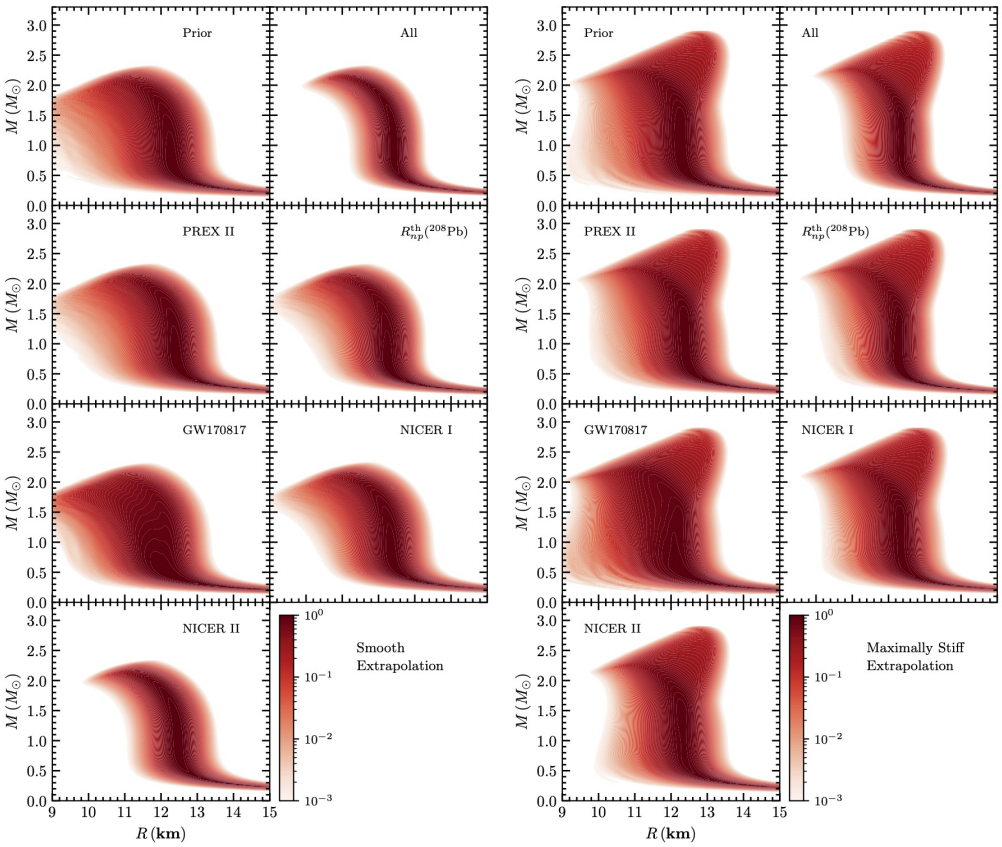

Figure 3. The mass-radius probability densities (priors, individual posteriors, and combined posteriors) from the smooth high-density extrapolation (**left**) and the maximally-stiff high-density extrapolation (**right**) energy density functionals.

In Figures 4 and 5 we show the $R_{1.4}$ and $R_{2.0}$ probability densities when the smooth high-density extrapolation (left) and maximally-stiff high-density extrapolation (right) are employed. The blue shaded regions represents the prior distributions, while the gray shaded regions represents the final posterior distributions when all likelihood functions are

combined. The other curves include only the effects of single likelihood functions (labeled in the figure) and thus can be used to evaluate the relative strengths of the individual experimental, theoretical, and observational constraints. From Figures 4 and 5 it is evident that GW170817 strongly favors soft equations of state, significantly shifting the distributions towards smaller radii for both $1.4\,M_\odot$ and $2.0\,M_\odot$ neutron stars. In the left panels of Figures 4 and 5, one also sees the importance of heavy neutron stars and the NICER II constraint when our nuclear theory models are extrapolated without modification into the high-density regime. The NICER II observation has less impact in the maximally-stiff high-density scenario since equations of state that are soft around $n \sim 2n_0$ can be made sufficiently stiff at high densities to support heavy neutron stars. Instead, for the maximally-stiff high density assumption, the PREX-II neutron skin thickness constraint plays the largest role in eliminating soft equations of state. These observations highlight the general fact that the impact of heavy neutron star observations on theoretical modeling depends sensitively on the choice of the high-density equation of state.

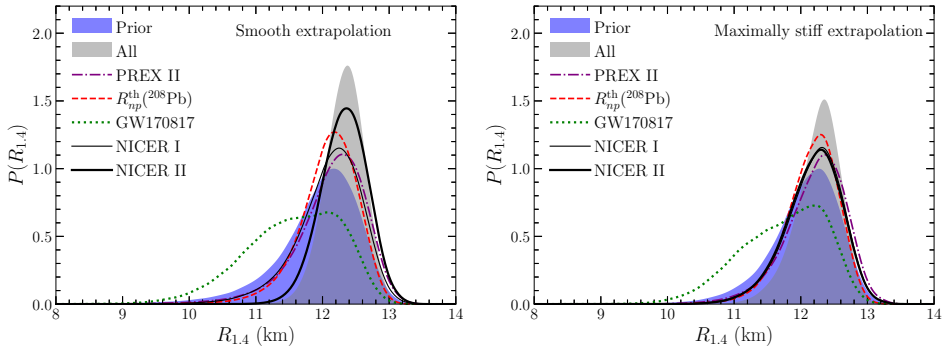

Figure 4. The $R_{1.4}$ probability densities (priors, individual posteriors, and combined posteriors) from the smooth high-density extrapolation (**left**) and the maximally-stiff high-density extrapolation (**right**) energy density functionals.

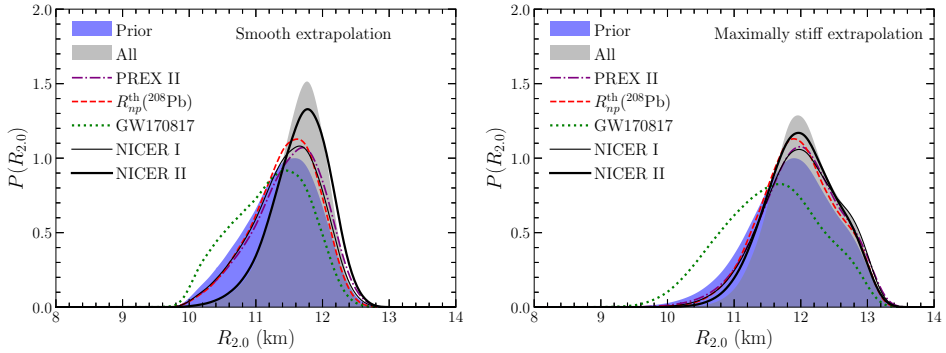

Figure 5. The $R_{2.0}$ probability densities (priors, individual posteriors, and combined posteriors) from the smooth high-density extrapolation (**left**) and the maximally-stiff high-density extrapolation (**right**) energy density functionals.

In Table 2 we show the most probable $R_{1.4}$ values, the 68% credibility intervals, and the 90% credibility intervals for the prior and posterior probability distributions assuming either the smooth or maximally-stiff high-density prior. When we employ the smooth high-density extrapolation, we see that the 90% uncertainty spread is reduced from 2.01 km (prior) to 0.96 km (posterior), which represents a dramatic reduction in the allowed radii of $1.4\,M_\odot$ neutron stars. This is due to competing likelihood functions, some of which favor stiff and others that favor soft equations of state. However, the 90% credibility range of $R_{1.4} = 12.38^{+0.39}_{-0.57}$ km is sufficiently large that there is no strong tension between present nuclear physics and neutron star observational constraints. For the maximally-stiff high-density extrapolation, the 90% credibility range for the prior spans 1.69 km while the

posterior is reduced to 1.11 km. The combined set of likelihood functions result in a nearly equal range of allowed radii in the two posteriors, with the maximally-stiff extrapolation allowing for a somewhat larger set of soft equations of state around twice saturation density.

Previous works have found results for $R_{1.4}$ that are consistent with our analysis. For instance, the first estimations of $R_{1.4}$ inferred from GW170817 found $R_{1.4} < 13.6$ km [16], 8.9 km $< R_{1.4} <$ 13.2 km [35] across all choices of their mass prior, 10.4 km $< R_{1.4} <$ 12.8 km [18], and $R_{1.4} = 11.9^{+1.4}_{-1.4}$ km [5] assuming a common equation of state for both neutron stars that can support the heaviest observed pulsars. Including also electromagnetic (EM) counterpart data from GW170817, Radice and Dai found $R_{1.4} = 12.2^{+1.0}_{-0.8} \pm 0.2$ km [75], while Capano et al. found $R_{1.4} = 11.0^{+0.9}_{-0.6}$ km [21], where the EM data were particularly important in setting a more stringent lower bound on the radius. Following work that included constraints from NICER observations of PSR J0030+0451 found $R_{1.4} = 12.54^{+0.71}_{-0.63}$ km [76], and including also NICER observations of PSR J0740+6620 resulted in $R_{1.4} = 12.33^{+0.76}_{-0.81}$ km [77] for a piecewise polytrope expansion of the high-density equation of state, $R_{1.4} = 12.45^{+0.65}_{-0.65}$ km [8] as the 1σ credible interval consistent with three different equation of state modeling assumptions, $R_{1.4} = 12.64^{+0.71}_{-0.88}$ km [25] based on the Riley et al. [9] posteriors, and $R_{1.4} = 12.34^{+1.01}_{-1.25}$ km [78] also based on the posteriors of Ref. [9], all of which are strongly consistent with our analysis.

Table 2. The 68% and 90% credibility ranges for $R_{1.4}$ associated with the smooth and maximally-stiff high-density priors as well as the two posteriors accounting for all likelihood functions included in this work.

	$R_{1.4}(68\%)$[km]	$R_{1.4}(90\%)$ [km]
Prior (Smooth)	$12.16^{+0.34}_{-0.78}$	$12.16^{+0.59}_{-1.42}$
Prior (Stiff)	$12.28^{+0.26}_{-0.71}$	$12.28^{+0.49}_{-1.2}$
Post. (Smooth)	$12.38^{+0.23}_{-0.35}$	$12.38^{+0.39}_{-0.57}$
Post. (Stiff)	$12.36^{+0.22}_{-0.44}$	$12.36^{+0.38}_{-0.73}$

Table 3. The 68% and 90% credibility ranges for $R_{2.0}$ associated with the smooth and maximally-stiff high-density priors as well as the two posteriors accounting for all likelihood functions included in this work.

	$R_{2.0}(68\%)$[km]	$R_{2.0}(90\%)$ [km]
Prior (Smooth)	$11.58^{+0.35}_{-0.79}$	$11.58^{+0.61}_{-1.19}$
Prior (Stiff)	$11.90^{+0.64}_{-0.67}$	$11.90^{+0.97}_{-1.15}$
Post. (Smooth)	$11.76^{+0.27}_{-0.50}$	$11.76^{+0.46}_{-0.84}$
Post. (Stiff)	$11.96^{+0.65}_{-0.40}$	$11.96^{+0.94}_{-0.71}$

In Table 3 we show the numerical values for the $R_{2.0}$ probability distribution. As expected, small radii are disfavored mostly due to the PSR J0740+6620 radius analysis in our NICER II likelihood function. The width for the 90% credibility range decreases from 1.80 km (2.12 km) to 1.30 km (1.65 km) in case of the smooth (maximally stiff) high-density extrapolation. The uncertainty in the 90% width for $R_{2.0}$ is larger compared to the $R_{1.4}$ uncertainty width due to uncertainties in the dense matter composition and equation of state at the largest baryon number densities. The two posterior median values of $R_{2.0} = 11.76$ km and $R_{2.0} = 11.96$ km associated with the smooth and maximally-stiff high-density extrapolations are somewhat lower than other recent analyses. For instance, including observational constraints from GW170817 as well as the NICER mass-radius measurements of PSR J0030+0451 and PSR J0740+6620 with the Riley et al. posterior [9], it was found $R_{2.08} = 12.70^{+1.01}_{-1.25}$ km at the 90% confidence level [25] and $R_{2.08} = 12.35 \pm 0.75$ km [8] as the range that spans the 1σ credibility interval across all of their equation

of state models. Including the same observational data together with non-parametric modeling of the nuclear equation of state, the authors of Ref. [78] find $R_{2.0} = 12.09^{+1.07}_{-1.17}$ km.

Figure 6 shows the prior density (blue shaded band), individual posterior densities (lines), and combined posterior density (gray shaded band) for the tidal deformability of a 1.4 $M_\odot$ neutron star using both the smooth extrapolation prior (left) and the maximally stiff extrapolation prior (right). In general, the different likelihood functions have qualitatively similar effects on neutron star tidal deformabilities and radii (shown in Figure 4). This is due to the positive correlation between $\Lambda_{1.4}$ and $R_{1.4}$ as seen in Figure 2. In particular, the likelihood from GW170817 strongly favors low values for $\Lambda_{1.4}$ in both prior scenarios since it is more difficult to deform neutron stars with smaller radii. The ab initio theory prediction for the neutron skin thickness $R^{\rm th}_{np}(^{208}{\rm Pb})$ gives only a small shift in the peak of the $\Lambda_{1.4}$ distribution, since it is strongly consistent with our chiral effective field theory constraints on the nuclear equation of state. The other constraints (NICER I, NICER II, PREX-II) all give larger shifts toward higher tidal deformabilities. Interestingly, the large uncertainty in the PREX-II likelihood function leads to greater statistical weight at both high and low values of $\Lambda_{1.4}$ compared to most of the other likelihood functions. Overall, the maximally-stiff high-density extrapolation exhibits a wider range in $\Lambda_{1.4}$ than the smooth extrapolation case, but the two posteriors peak at similar values of $\Lambda_{1.4} \sim 440$. We also note that most likelihood functions have a smaller impact on the $\Lambda_{1.4}$ distribution in the maximally-stiff high-density extrapolation compared to the smooth extrapolation prior because of the greater flexibility in the maximally-stiff model. Nevertheless, for both priors the combined effects of all likelihoods is to shift the $\Lambda_{1.4}$ distribution to larger values as seen by comparing the blue-shaded and gray-shaded curves.

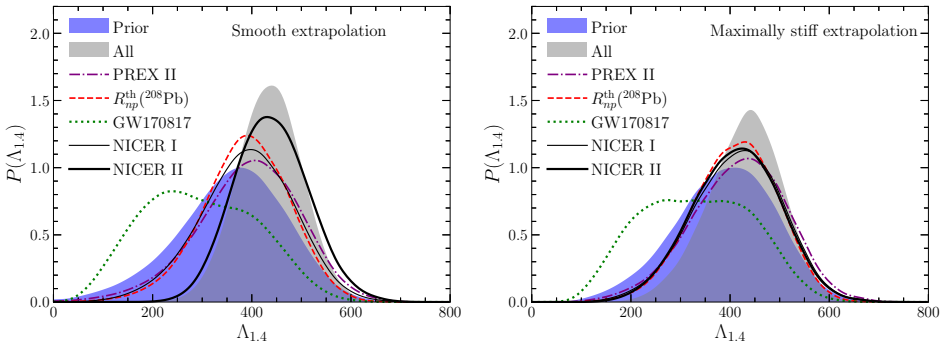

Figure 6. The $\Lambda_{1.4}$ probability densities (priors, individual posteriors, and combined posteriors) from the smooth high-density extrapolation (**left**) and the maximally-stiff high-density extrapolation (**right**) energy density functionals.

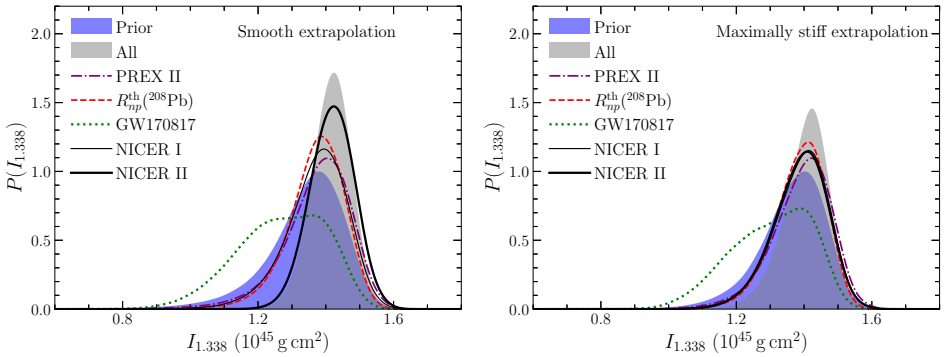

Figure 7. The $I_{1.338}$ probability densities (priors, individual posteriors, and combined posteriors) from the smooth high-density extrapolation (**left**) and the maximally-stiff high-density extrapolation (**right**) energy density functionals.

Table 4 shows the most likely value of $\Lambda_{1.4}$ as well as the 68% and 90% credibility ranges under the smooth and maximally-stiff high-density extrapolations. The two prior probability distributions are already strongly consistent with the constraint $\Lambda_{1.4} = 190^{+390}_{-120}$ from GW170817 [5] obtained when a common equation of state is used to model the two progenitor neutron stars. We note that the result from Ref. [5] also does not include the existence of heavy $\sim 2\,M_\odot$ neutron stars as a constraint. The largest difference between our prior models and the analysis [5] of GW170817 is that the latter cannot strongly constrain the lower bound of the tidal deformability, whereas chiral effective field theory calculations exclude the extremely soft equations of state that would be needed to reach values of the tidal deformability $\Lambda_{1.4} < 150$. The 90% credibility ranges for the smooth and maximally-stiff high-density priors have uncertainties of 370 and 330, respectively, whereas the posteriors have uncertainties of 210 and 250. Again, we find that the smooth high-density extrapolation has a larger spread in the prior but a smaller spread in the posterior, primarily due to the strong constraints from NICER II and the existence of massive $\sim 2\,M_\odot$ neutron stars. Interestingly, the two posteriors have the same peak value of $\Lambda = 440$ and quite similar uncertainties, indicating that the posterior is not dominated by the choice of prior. Our results are consistent with previous analyses that included a range of observational constraints. With a completely agnostic prior, it was found [76] that including only data from GW170817 the tidal deformability of a $1.4\,M_\odot$ neutron star lies in the range $\Lambda_{1.4} = 228^{+319}_{-134}$ and including also NICER measurements of PSR J0030+0451 $\Lambda_{1.4} = 451^{+241}_{-279}$. With priors tightly constrained on realistic neutron star equations of state from the literature, a somewhat smaller range of $\Lambda_{1.4} = 491^{+216}_{-181}$ was found [79]. With the inclusion of chiral effective field theory constraints on the equation of state up to $2n_0$ as well as constraints from NICER observations of PSR J0030+0451, the authors of Ref. [76] find a much reduced range $\Lambda_{1.4} = 465^{+125}_{-177}$. Finally, several works have also included constraints from NICER-XMM observations of PSR J0740+6620 to obtain e.g., $\Lambda_{1.4} = 575^{+262}_{-232}$ [25] using the Miller et al. [8] posteriors and $\Lambda_{1.4} = 457^{+219}_{-256}$ [78] using the Riley et al. [9] posteriors. These distributions peak at larger central values of $\Lambda_{1.4}$ and have larger uncertainties compared to our analysis primarily due to their use of nuclear-physics-agnostic parameterizations of the neutron star equation of state.

Table 4. The 68% and 90% credibility ranges for $\Lambda_{1.4}$ associated with the smooth and maximally-stiff high-density priors as well as the two posteriors accounting for all likelihood functions included in this work.

	$\boldsymbol{\Lambda_{1.4}(68\%)}$	$\boldsymbol{\Lambda_{1.4}(90\%)}$
Prior (Smooth)	376^{+91}_{-129}	376^{+151}_{-216}
Prior (Stiff)	408^{+81}_{-123}	408^{+136}_{-195}
Post. (Smooth)	440^{+60}_{-71}	440^{+101}_{-113}
Post. (Stiff)	440^{+61}_{-89}	440^{+103}_{-144}

In Figure 7 we show the prior density (blue shaded band), individual posterior densities (lines), and combined posterior density (gray shaded band) for the moment of inertia $I_{1.338}$ of PSR J0737-3039A using both the smooth high-density extrapolation (left) and the maximally stiff high-density extrapolation (right). The neutron star moment of inertia is strongly correlated with both the radius and tidal deformability, and therefore the trends observed in the two latter cases (see Figures 4 and 6) are also exhibited by the moment of inertia. Like the radius $R_{1.4}$ and tidal deformability $\Lambda_{1.4}$, the probability distribution of $I_{1.338}$ is not symmetric about its peak value but instead has a longer tail toward small values. The ab initio theory prediction for the ^{208}Pb neutron skin thickness eliminates a small fraction of the softest equations of state and stiffest equations of state such that the peak of the distribution is nearly the same as that of the prior. Comparatively, the PREX-II neutron skin thickness measurement gives rise to longer tails at both low and high values

of the moment of inertia. Both posteriors, however, have very similar peak values and uncertainty widths.

In Table 5 we show the most likely value of $I_{1.338}$ as well as the 68% and 90% credibility ranges under the smooth and maximally-stiff high-density extrapolations. Recently, Kramer et al. [80] have obtained the value $I_{1.338} < 3 \times 10^{45}\,\mathrm{g\,cm^2}$ at the 90% credibility level for the moment of inertia of PSR J0737-3039A. We see that all of our models satisfy this upper bound on the moment of inertia and in fact lie much below the empirical upper bound. Landry and Kumar [81] obtained $I_{1.338} = 1.15^{+0.38}_{-0.24} \times 10^{45}\mathrm{g\,cm^2}$ from neutron star universal relations [82] linking the neutron star tidal deformability and moment of inertia. Recently, Greif et al. [39] obtained $1.058 < I_{1.338} < 1.708 \times 10^{45}\mathrm{g\,cm^2}$ from the speed of sound model and piecewise polytropic model constrained by chiral effective field theory and neutron star observables. Compared with all of these works, our posterior analysis gives a considerably smaller 90% credibility width of 0.19 and $0.22 \times 10^{45}\mathrm{g\,cm^2}$ from the smooth extrapolation and maximally-stiff extrapolation posteriors, respectively. The probability density for $I_{1.338}$ peaks around $1.43 \times 10^{45}\,\mathrm{g\,cm^2}$ under both high-density models. The net effect of all likelihood functions is to reduce the uncertainty while only slightly increasing the peak of the $I_{1.338}$ distribution.

Table 5. The 68% and 90% credibility ranges for $I_{1.338}$ (in units of $10^{45}\,\mathrm{g\,cm^2}$) associated with the smooth and maximally-stiff high-density priors as well as the two posteriors accounting for all likelihood functions included in this work.

	$I_{1.338}(68\%)$	$I_{1.338}(90\%)$
Prior (Smooth)	$1.375^{+0.068}_{-0.143}$	$1.375^{+0.118}_{-0.260}$
Prior (Stiff)	$1.400^{+0.056}_{-0.132}$	$1.400^{+0.100}_{-0.221}$
Post. (Smooth)	$1.430^{+0.039}_{-0.071}$	$1.430^{+0.074}_{-0.115}$
Post. (Stiff)	$1.425^{+0.041}_{-0.089}$	$1.425^{+0.074}_{-0.146}$

5. Discussion

We have studied the impact of recent theoretical and experimental investigations of the neutron skin thickness of ^{208}Pb on predicted neutron star radii, tidal deformabilities, and moments of inertia. These have been included in a comprehensive Bayesian statistical analysis that also includes constraints from chiral effective field theory, properties of medium-mass and heavy nuclei, and astronomical observations of neutron star radii and tidal deformabilities. We have employed two choices for the high-density equation of state and find that the associated posteriors are very similar and do not depend sensitively on this choice. We find that the ab initio nuclear theory calculation of $R_{np}^{\mathrm{th}}(^{208}\mathrm{Pb})$ narrows the uncertainty in neutron star properties without strongly modifying the peak probabilities for radii, deformabilities, and moments of inertia. In comparison, the PREX-II experimental determination of $R_{np}^{\mathrm{exp}}(^{208}\mathrm{Pb})$ leads to broader posterior distributions for neutron star properties that are peaked at larger central values but also have longer tails toward the minima of the distributions. Given the large allowed space of posterior equations of state from the smooth high-density extrapolation scenario, it is not yet necessary to introduce phase transitions or hyperonic degrees of freedom in neutron stars to accommodate all current constraints [28,83–87], though such exotic states are also not ruled out in our analysis. Our present modeling can be further refined through future measurements of neutron-rich nuclei at rare-isotope beam facilities, ab initio nuclear theory calculations, and neutron star observations.

Author Contributions: Conceptualization, Y.L. and J.W.H.; methodology, Y.L. and J.W.H.; software, Y.L.; validation, Y.L. and J.W.H.; formal analysis, Y.L. and J.W.H.; investigation, Y.L. and J.W.H.; resources, Y.L. and J.W.H.; data curation, Y.L.; writing—original draft preparation, Y.L.; writing—review and editing, Y.L. and J.W.H.; visualization, Y.L. and J.W.H.; supervision, Y.L. and J.W.H.; project administration, Y.L. and J.W.H.; funding acquisition, Y.L. and J.W.H. All authors have read and agreed to the published version of the manuscript.

Funding: This research was funded by Ewha Womans University Research Grant of 2021(1-2021-0520-001-1), the National Research Foundation of Korea (NRF) grant funded by the Korea government (MSIT) (No. 2021R1A2C2094378), the US National Science Foundation Grant No. PHY1652199 and the U.S. Department of Energy National Nuclear Security Administration Grant No. DE-NA0003841.

Institutional Review Board Statement: Not applicable.

Informed Consent Statement: Not applicable.

Data Availability Statement: Data from this study will be provided upon request by Y.L.

Acknowledgments: We thank Baishan Hu and Christian Forssen for providing posterior equation of state samples associated with the theoretical determination of the ^{208}Pb neutron skin thickness. Portions of this research were conducted with the advanced computing resources provided by Texas A&M High Performance Research Computing.

Conflicts of Interest: The authors declare no conflict of interest.

References

1. Demorest, P.; Pennucci, T.; Ransom, S.; Roberts, M.; Hessels, J. A Two-Solar-Mass Neutron Star Measured using Shapiro Delay. *Nature* **2010**, *467*, 1081. [CrossRef] [PubMed]
2. Antoniadis, J.; Freire, P.C.C.; Wex, N.; Tauris, T.M.; Lynch, R.S.; van Kerkwijk, M.H.; Kramer, M.; Bassa, C.; Dhillon, V.S.; Driebe, T.; et al. A Massive Pulsar in a Compact Relativistic Binary. *Science* **2013**, *340*, 6131. [CrossRef] [PubMed]
3. Cromartie, H.T.; Fonseca, E.; Ransom, S.M.; Demorest, P.B.; Arzoumanian, Z.; Blumer, H.; Brook, P.R.; DeCesar, M.E.; Dolch, T.; Ellis, J.A.; et al. Relativistic Shapiro Delay Measurements of an Extremely Massive Millisecond Pulsar. *Nat. Astron.* **2019**, *4*, 72. [CrossRef]
4. Abbott, B.P.; Abbott, R.; Abbott, T.D.; Acernese, F.; Ackley, K.; Adams, C.; Adams, T.; Addesso, P.; Adhikari, R.X.; Adya, V.B.; et al. [LIGO Scientific Collaboration and Virgo Collaboration]. GW170817: Observation of Gravitational Waves from a Binary Neutron Star Inspiral. *Phys. Rev. Lett.* **2017**, *119*, 161101. [CrossRef] [PubMed]
5. Abbott, B.P.; Abbott, R.; Abbott, T.D.; Acernese, F.; Ackley, K.; Adams, C.; Adams, T.; Addesso, P.; Adhikari, R.X.; Adya, V.B.; et al. [The LIGO Scientific Collaboration and the Virgo Collaboration]. GW170817: Measurements of Neutron Star Radii and Equation of State. *Phys. Rev. Lett.* **2018**, *121*, 161101. [CrossRef] [PubMed]
6. Miller, M.C.; Lamb, F.K.; Dittmann, A.J.; Bogdanov, S.; Arzoumanian, Z.; Gendreau, K.C.; Guillot, S.; Harding, A.K.; Ho, W.C.G.; Lattimer, J.M.; et al. PSR J0030+0451 Mass and Radius from NICER Data and Implications for the Properties of Neutron Star Matter. *Astrophys. J.* **2019**, *887*, L24. [CrossRef]
7. Riley, T.E.; Watts, A.L.; Bogdanov, S.; Ray, P.S.; Ludlam, R.M.; Guillot, S.; Arzoumanian, Z.; Baker, C.L.; Bilous, A.V.; Chakrabarty, D.; et al. A NICER View of PSR J0030+0451: Millisecond Pulsar Parameter Estimation. *Astrophys. J.* **2019**, *887*, L21. [CrossRef]
8. Miller, M.C.; Lamb, F.K.; Dittmann, A.J.; Bogdanov, S.; Arzoumanian, Z.; Gendreau, K.C.; Guillot, S.; Ho, W.C.G.; Lattimer, J.M.; Loewenstein, M.; et al. The Radius of PSR J0740+6620 from NICER and XMM-Newton Data. *Astrophys. J. Lett.* **2021**, *918*, L28. [CrossRef]
9. Riley, T.E.; Watts, A.L.; Ray, P.S.; Bogdanov, S.; Guillot, S.; Morsink, S.M.; Bilous, A.V.; Arzoumanian, Z.; Choudhury, D.; Deneva, J.S.; et al. A NICER View of the Massive Pulsar PSR J0740+6620 Informed by Radio Timing and XMM-Newton Spectroscopy. *Astrophys. J. Lett.* **2021**, *918*, L27. [CrossRef]
10. Essick, R.; Landry, P.; Schwenk, A.; Tews, I. Detailed Examination of Astrophysical Constraints on the Symmetry Energy and the Neutron Skin of ^{208}Pb with Minimal Modeling Assumptions. *Phys. Rev. C* **2021**, *104*, 065804. [CrossRef]
11. Li, B.-A.; Cai, B.-J.; Xie, W.-J.; Zhang, N.-B. Progress in Constraining Nuclear Symmetry Energy Using Neutron Star Observables Since GW170817. *Universe* **2021**, *7*, 182. [CrossRef]
12. Drischler, C.; Holt, J.W.; Wellenhofer, C. Chiral Effective Field Theory and the High-Density Nuclear Equation of State. *Ann. Rev. Nucl. Part. Sci.* **2021**, *71*, 403. [CrossRef]
13. Epelbaum, E.; Hammer, H.-W. ; Meißner, U.-G. Modern Theory of Nuclear Forces. *Rev. Mod. Phys.* **2009**, *81*, 1773. [CrossRef]
14. Machleidt, R.; Entem, D.R. Chiral Effective Field Theory and Nuclear Forces. *Phys. Rept.* **2011**, *503*, 1. [CrossRef]
15. Hebeler, K.; Lattimer, J.M.; Pethick, C.J. ; Schwenk, A. Constraints on Neutron Star Radii Based on Chiral Effective Field Theory Interactions. *Phys. Rev. Lett.* **2010**, *105*, 161102. [CrossRef]
16. Annala, E.; Gorda, T.; Kurkela, A.; Vuorinen, A. Gravitational-Wave Constraints on the Neutron-Star-Matter Equation of State. *Phys. Rev. Lett.* **2018**, *120*, 172703. [CrossRef]

17. Most, E.R.; Weih, L.R.; Rezzolla, L.; Schaffner-Bielich, J. New Constraints on Radii and Tidal Deformabilities of Neutron Stars from GW170817. *Phys. Rev. Lett.* **2018**, *120*, 261103. [CrossRef]
18. Lim, Y.; Holt, J.W. Neutron Star Tidal Deformabilities Constrained by Nuclear Theory and Experiment. *Phys. Rev. Lett.* **2018**, *121*, 062701. [CrossRef]
19. Tews, I.; Margueron, J. ; Reddy, S. Critical Examination of Constraints on the Equation of State of Dense Matter Obtained from GW170817. *Phys. Rev. C* **2018**, *98*, 045804. [CrossRef]
20. Lim, Y.; Holt, J.W. Bayesian Modeling of the Nuclear Equation of State for Neutron Star Tidal Deformabilities and GW170817. *Eur. Phys. J. A* **2019**, *55*, 209. [CrossRef]
21. Capano, C.D.; Tews, I.; Brown, S.M.; Margalit, B.; De, S.; Kumar, S.; Brown, D.A.; Krishnan, B.; Reddy, S. Stringent Constraints on Neutron-Star Radii from Multimessenger Observations and Nuclear Theory. *Nat. Astron.* **2020**, *4*, 625. [CrossRef]
22. Drischler, C.; Han, S.; Lattimer, J.M.; Prakash, A.M.; Reddy, S.; Zhao, T. Limiting Masses and Radii of Neutron Stars and Their Implications. *Phys. Rev. C* **2021**, *103*, 045808. [CrossRef]
23. Adhikari, D.; Albataineh, H.; Androic, D.; Aniol, K.; Armstrong, D.S.; Averett, T.; Barcus, S.; Bellini, V.; Beminiwattha, R.S.; [PREX Collaboration]; et al. Accurate Determination of the Neutron Skin Thickness of ^{208}Pb through Parity-Violation in Electron Scattering. *Phys. Rev. Lett.* **2021**, *126*, 172502. [CrossRef] [PubMed]
24. Reed, B.T.; Fattoyev, F.J.; Horowitz, C.J.; Piekarewicz, J. Implications of PREX-2 on the Equation of State of Neutron-Rich Matter. *Phys. Rev. Lett.* **2021**, *126*, 172503. [CrossRef]
25. Biswas, B. Impact of PREX-II and Combined Radio/NICER/XMM-Newton's Mass–Radius Measurement of PSR J0740+6620 on the Dense-matter Equation of State. *Astrophys. J.* **2021**, *921*, 63. [CrossRef]
26. Hu, B.; Jiang, W.; Miyagi, T.; Sun, Z.; Ekström, A.; Forssén, C.; Hagen, G.; Holt, J.D.; Papenbrock, T.; Stroberg, S.R.; et al. Ab Initio Predictions Link the Neutron Skin of ^{208}Pb to Nuclear Forces. *arXiv* **2021**, arXiv:2112.01125.
27. Schulze, H.-J.; Rijken, T. Maximum Mass of Hyperon Stars with the Nijmegen ESC08 Model. *Phys. Rev. C* **2011**, *84*, 035801. [CrossRef]
28. Lonardoni, D.; Lovato, A.; Gandolfi, S.; Pederiva, F. Hyperon Puzzle: Hints from Quantum Monte Carlo Calculations. *Phys. Rev. Lett.* **2015**, *114*, 092301. [CrossRef]
29. Rijken, T.A.; Nagels, M.M.; Yamamoto, Y. Status of Understanding the YN/YY-Interactions Meson-Exchange Viewpoint. *Nucl. Phys.* **2010** *A835*, 160. [CrossRef]
30. Lonardoni, D.; Gandolfi, S.; Pederiva, F. Effects of the Two-Body and Three-Body Hyperon-Nucleon Interactions in Λ-Hypernuclei. *Phys. Rev. C* **2013**, *87*, 041303. [CrossRef]
31. Petschauer, S.; Haidenbauer, J.; Kaiser, N.; Meissner, U.-G.; Weise, W. Hyperon-Nuclear Interactions from SU(3) Chiral Effective Field Theory. *Front. Phys.* **2020**, *8*, 12. [CrossRef]
32. Gerstung, D.; Kaiser, N.; Weise, W. Hyperon-Nucleon Three-Body Forces and Strangeness in Neutron Stars. *Eur. Phys. J. A* **2020**, *56*, 175. [CrossRef]
33. Abbott, B.P.; Abbott, R.; Abbott, T.D.; Acernese, F.; Ackley, K.; Adams, C.; Adams, T.; Addesso, P.; Adhikari, R.X.; Adya, V.B.; et al. Multi-messenger Observations of a Binary Neutron Star Merger. *Astrophys. J. Lett.* **2017**, *848*, L12. [CrossRef]
34. Bauswein, A.; Bastian, N.-U.F.; Blaschke, D.B.; Chatziioannou, K.; Clark, J.A.; Fischer, T.; Oertel, M. Identifying a First-Order Phase Transition in Neutron-Star Mergers through Gravitational Waves. *Phys. Rev. Lett.* **2019**, *122*, 061102. [CrossRef]
35. De, S.; Finstad, D.; Lattimer, J.M.; Brown, D.A.; Berger, E.; Biwer, C.M. Tidal Deformabilities and Radii of Neutron Stars from the Observation of GW170817. *Phys. Rev. Lett.* **2018**, *121*, 091102. [CrossRef]
36. Itoh, N. Hydrostatic Equilibrium of Hypothetical Quark Stars. *Prog. Theor. Phys.* **1970**, *44*, 291. [CrossRef]
37. Tews, I.; Carlson, J.; Gandolfi, S.; Reddy, S. Constraining the Speed of Sound Inside Neutron Stars with Chiral Effective Field Theory Interactions and Observations. *Astrophys. J.* **2018**, *860*, 149. [CrossRef]
38. Lim, Y.; Holt, J.W.; Stahulak, R.J. Predicting the Moment of Inertia of Pulsar J0737-3039A from Bayesian Modeling of the Nuclear Equation of State. *Phys. Rev. C* **2019**, *100*, 035802. [CrossRef]
39. Greif, S.; Hebeler, K.; Lattimer, J.; Pethick, C.; Schwenk, A. Equation of State Constraints from Nuclear Physics, Neutron Star Masses, and Future Moment of Inertia Measurements. *Astrophys. J.* **2020**, *901*, 155. [CrossRef]
40. Tsang, M.B.; Stone, J.R.; Camera, F.; Danielewicz, P.; Gandolfi, S.; Hebeler, K.; Horowitz, C.J.; Lee, J.; Lynch, W.G.; Kohley, Z.; et al. Constraints on the Symmetry Energy and Neutron Skins from Experiments and Theory. *Phys. Rev. C* **2012**, *86*, 015803. [CrossRef]
41. Lattimer, J.M.; Lim, Y. Constraining the Symmetry Parameters of the Nuclear Interaction. *Astrophys. J.* **2013**, *771*, 51. [CrossRef]
42. Holt, J.W.; Kaiser, N. Equation of State of Nuclear and Neutron Matter at Third-Order in Perturbation Theory from Chiral Effective Field Theory. *Phys. Rev. C* **2017**, *95*, 034326. [CrossRef]
43. Somasundaram, R.; Drischler, C.; Tews, I.; Margueron, J. Constraints on the Nuclear Symmetry Energy from Asymmetric-Matter Calculations with Chiral NN and $3N$ Interactions. *Phys. Rev. C* **2021**, *103*, 045803. [CrossRef]
44. Sammarruca, F.; Millerson, R. Analysis of the Neutron Matter Equation of State and the Symmetry Energy up to Fourth Order of Chiral Effective Field Theory. *Phys. Rev. C* **2021**, *104*, 034308. [CrossRef]
45. Danielewicz, P.; Lacey, R.; Lynch, W.G. Determination of the Equation of State of Dense Matter. *Science* **2002**, *298*, 1592. [CrossRef] [PubMed]
46. Shetty, D.V.; Yennello, S.J.; Botvina, A.S.; Souliotis, G.A.; Jandel, M.; Bell, E.; Keksis, A.; Soisson, S.; Stein, B.; Iglio, J. Symmetry Energy and the Isospin Dependent Equation of State. *Phys. Rev. C* **2004**, *70*, 011601. [CrossRef]

47. Estee, J.; Lynch, W.G.; Tsang, C.Y.; Barney, J.; Jhang, G.; Tsang, M.B.; Wang, R.; Kaneko, M.; Lee, J.W.; Isobe, T.; et al. Probing the Symmetry Energy with the Spectral Pion Ratio. *Phys. Rev. Lett.* **2021**, *126*, 162701. [CrossRef] [PubMed]
48. Reinhard, P.-G.; Roca-Maza, X.; Nazarewicz, W. Information Content of the Parity-Violating Asymmetry in ^{208}Pb. *Phys. Rev. Lett.* **2021**, *127*, 232501. [CrossRef]
49. Lim, Y.; Bhattacharya, A.; Holt, J.W.; Pati, D. Radius and Equation of State Constraints from Massive Neutron Stars and GW190814. *Phys. Rev. C* **2021**, *104*, L032802. [CrossRef]
50. Lim, Y.; Holt, J.W. Structure of Neutron Star Crusts from New Skyrme Effective Interactions Constrained by Chiral Effective Field Theory. *Phys. Rev. C* **2017**, *95*, 065805. [CrossRef]
51. Hebeler, K.; Schwenk, A. Chiral Three-Nucleon Forces and Neutron Matter. *Phys. Rev. C* **2010**, *82*, 014314. [CrossRef]
52. Drischler, C.; Carbone, A.; Hebeler, K.; Schwenk, A. Neutron Matter from Chiral Two- and Three-Nucleon Calculations up to N3LO. *Phys. Rev. C* **2016**, *94*, 054307. [CrossRef]
53. Drischler, C.; Hebeler, K.; Schwenk, A. Asymmetric Nuclear Matter Based on Chiral Two- and Three-Nucleon Interactions. *Phys. Rev. C* **2016**, *93*, 054314. [CrossRef]
54. Wellenhofer, C.; Holt, J.W.; Kaiser, N. Divergence of the Isospin-Asymmetry Expansion of the Nuclear Equation of State in Many-Body Perturbation Theory. *Phys. Rev. C* **2016**, *93*, 055802 [CrossRef]
55. Drischler, C.; Hebeler, K.; Schwenk, A. Chiral Interactions up to Next-to-Next-to-Next-to-Leading Order and Nuclear Saturation. *Phys. Rev. Lett.* **2019**, *122*, 042501. [CrossRef]
56. Gezerlis, A.; Tews, I.; Epelbaum, E.; Gandolfi, S.; Hebeler, K.; Nogga, A.; Schwenk, A. Quantum Monte Carlo Calculations with Chiral Effective Field Theory Interactions. *Phys. Rev. Lett.* **2013**, *111*, 032501. [CrossRef]
57. Roggero, A.; Mukherjee, A.; Pederiva, F. Quantum Monte Carlo Calculations of Neutron Matter with Nonlocal Chiral Interactions. *Phys. Rev. Lett.* **2014**, *112*, 221103. [CrossRef]
58. Wlazlowski, G.; Holt, J.W.; Moroz, S.; Bulgac, A.; Roche, K. Auxiliary-Field Quantum Monte Carlo Simulations of Neutron Matter in Chiral Effective Field Theory. *Phys. Rev. Lett.* **2014**, *113*, 182503. [CrossRef]
59. Tews, I.; Gandolfi, S.; Gezerlis, A.; Schwenk, A. Quantum Monte Carlo Calculations of Neutron Matter with Chiral Three-Body Forces. *Phys. Rev. C* **2016**, *93*, 024305. [CrossRef]
60. Carbone, A.; Rios, A.; Polls, A. Correlated Density-Dependent Chiral Forces for Infinite-Matter Calculations within the Green's Function Approach. *Phys. Rev. C* **2014**, *90*, 054322. [CrossRef]
61. Huang, W.; Wang, M.; Kondev, F.; Audi, G.; Naimi, S. The AME 2020 atomic mass evaluation (I). Evaluation of Input Data, and Adjustment Procedures. *Chin. Phys. C* **2021**, *45*, 030002. [CrossRef]
62. Coraggio, L.; Holt, J.W.; Itaco, N.; Machleidt, R.; Sammarruca, F. Reduced Regulator Dependence of Neutron-Matter Predictions with Perturbative Chiral Interactions. *Phys. Rev. C* **2013**, *87*, 014322. [CrossRef]
63. Kaiser, N. Quartic Isospin Asymmetry Energy of Nuclear Matter from Chiral Pion-Nucleon Dynamics. *Phys. Rev. C* **2015**, *91*, 065201. [CrossRef]
64. Wen, P.; Holt, J.W. Constraining the Nonanalytic Terms in the Isospin-Asymmetry Expansion of the Nuclear Equation of State. *Phys. Rev. C* **2021**, *103*, 064002. [CrossRef]
65. Lagaris, I.E.; Pandharipande, V.R. Variational Calculations of Asymmetric Nuclear Matter. *Nucl. Phys.* **1981**, *A369*, 470. [CrossRef]
66. Bombaci, I.; Lombardo, U. Asymmetric Nuclear Matter Equation of State. *Phys. Rev. C* **1991**, *44*, 1892. [CrossRef] [PubMed]
67. Drischler, C.; Furnstahl, R.J.; Melendez, J.A.; Phillips, D.R. How Well Do We Know the Neutron-Matter Equation of State at the Densities Inside Neutron Stars? A Bayesian Approach with Correlated Uncertainties. *Phys. Rev. Lett.* **2020**, *125*, 202702. [CrossRef]
68. Dutra, M.; Lourenco, O.; Sá Martins, J.S.; Delfino, A.; Stone, J.R.; Stevenson, P.D. Skyrme Interaction and Nuclear Matter Constraints. *Phys. Rev. C* **2012**, *85*, 035201. [CrossRef]
69. Tews, I.; Lattimer, J.M.; Ohnishi, A.; Kolomeitsev, E.E. Symmetry Parameter Constraints from a Lower Bound on Neutron-matter Energy. *Astrophys. J.* **2017**, *848*, 105. [CrossRef]
70. Holt, J.W.; Lim, Y. Universal Correlations in the Nuclear Symmetry Energy, Slope Parameter, and Curvature. *Phys. Lett.* **2018**, *B784*, 77. [CrossRef]
71. Margueron, J.; Gulminelli, F. Effect of High-Order Empirical Parameters on the Nuclear Equation of State. *Phys. Rev. C* **2019**, *99*, 025806. [CrossRef]
72. Lattimer, J.M.; Swesty, F.D. A Generalized Equation of State for Hot, Dense Matter. *Nucl. Phys.* **1991**, *A535*, 331. [CrossRef]
73. Gandolfi, S.; Carlson, J.; Reddy, S. Maximum Mass and Radius of Neutron Stars, and the Nuclear Symmetry Energy. *Phys. Rev. C* **2012**, *85*, 032801. [CrossRef]
74. Abbott, B.P.; Abbott, R.; Abbott, T.D.; Acernese, F.; Ackley, K.; Adams, C.; Adams, T.; Addesso, P.; Adhikari, R.X.; [LIGO Scientific Collaboration and Virgo Collaboration]; et al. Properties of the Binary Neutron Star Merger GW170817. *Phys. Rev. X* **2019**, *9*, 011001.
75. Radice, D.; Dai, L. Multimessenger Parameter Estimation of GW170817. *Eur. Phys. J. A* **2019**, *55*, 50. [CrossRef]
76. Essick, R.; Tews, I.; Landry, P.; Reddy, A.S.; Holz, D.E. Direct Astrophysical Tests of Chiral Effective Field Theory at Supranuclear Densities. *Phys. Rev. C* **2020**, *102*, 055803. [CrossRef]
77. Raaijmakers, G.; Greif, S.K.; Hebeler, K.; Hinderer, T.; Nissanke, a.S.; Schwenk, A.; Riley, T.E.; Watts, A.L.; Lattimer, J.M.; Ho, W.C.G. Constraints on the Dense Matter Equation of State and Neutron Star Properties from NICER's Mass-Radius Estimate of PSR J0740+6620 and Multimessenger Observations. *Astrophys. J. Lett.* **2021**, *918*, L29. [CrossRef]

78. Legred, I.; Chatziioannou, K.; Essick, R.; Han, S.; Landry, P. Impact of the PSR J0740+6620 Radius Constraint on the Properties of High-Density Matter. *Phys. Rev. D* **2021**, *104*, 063003. [CrossRef]
79. Essick, R.; Landry, P.; Holz, D.E. Nonparametric Inference of Neutron Star Composition, Equation of State, and Maximum Mass with GW170817. *Phys. Rev. D* **2020**, *101*, 063007. [CrossRef]
80. Kramer, M.; Stairs, I.H.; Manchester, R.N.; Wex, N.; Deller, A.T.; Coles, W.A.; Ali, M.; Burgay, M.; Camilo, F.; Cognard, I.; et al. Strong-Field Gravity Tests with the Double Pulsar. *Phys. Rev. X* **2021**, *11*, 041050. [CrossRef]
81. Landry, P.; Kumar, B. Constraints on the Moment of Inertia of PSR J0737-3039A from GW170817. *Astrophys. J.* **2018**, *868*, L22. [CrossRef]
82. Yagi, K.; Yunes, N. I-Love-Q Relations in Neutron Stars and Their Applications to Astrophysics, Gravitational Waves, and Fundamental Physics. *Phys. Rev. D* **2013**, *88*, 023009. [CrossRef]
83. Chamel, N.; Fantina, A.F.; Pearson, J.M.; Goriely, S. Phase Transitions in Dense Matter and the Maximum Mass of Neutron Stars. *Astron. Astrophys.* **2013**, *553*, A22. [CrossRef]
84. Han, S.; Steiner, A.W. Tidal Deformability with Sharp Phase Transitions in Binary Neutron Stars. *Phys. Rev. D* **2019**, *99*, 083014. [CrossRef]
85. Somasundaram, R.; Margueron, J. Impact of Massive Neutron Star Radii on the Nature of Phase Transitions in Dense Matter. *EPL* **2022**, *138*, 14002. [CrossRef]
86. Altiparmak, S.; Ecker, C.; Rezzolla, L. On the Sound Speed in Neutron Stars. *arXiv* **2022**, arXiv:2203.14974.
87. Brandes, L.; Weise, W.; Kaiser, N. Inference of the Sound Speed and Related Properties of Neutron Stars. *arXiv* **2022**, arXiv:2208.03026.